Experiments in Fluids 34 (2003) 504–514
DOI 10.1007/s00348-003-0588-y

Particle imaging techniques for microfabricated fluidic systems

S. Devasenathipathy, J.G. Santiago, S.T. Wereley, C.D. Meinhart, K. Takehara

Abstract This paper presents the design and implementation of velocimetry techniques applicable to the analysis of microfluidic systems. The application of both micron-resolution particle image velocimetry (micro-PIV) and particle tracking velocimetry (PTV) to the measurement of velocity fields within micromachined fluidic channels is presented. The particle tracking system uses epifluorescent microscopy, CCD imaging, and specialized image interrogation algorithms to provide microscale velocity measurement resolution. The flow field in a straight channel section is measured using cross-correlation micro-PIV and compared to the analytical solution for a measured mass flow rate. Velocity field measurements of the flow at the intersection of a cross-channel are also presented and compared with simulations from a commercially available flow solver, CFD-ACE+. Discussions regarding flow seeding, imaging optics, and the flow setup for measuring flows in microfabricated fluidic devices are presented. A simple process for estimating measurement uncertainty of the in-plane velocity measurements caused by three-dimensional Brownian motion is described. A definition for the measurement depth for PTV measurements is proposed. The agreement between measured and predicted values lends further support to the argument that liquid microflows with characteristic dimensions of order 50-μm dimension channels follow macroscale flow theory.

Received: 9 October 2001 / Accepted: 26 November 2002
Published online: 5 March 2003

S. Devasenathipathy (✉), J.G. Santiago
Department of Mechanical Engineering,
Thermosciences Division, Stanford University,
Building 500, Stanford, CA, 94305, USA
E-mail: dshankar@stanford.edu

S.T. Wereley
Department of Mechanical Engineering,
Purdue University, West Lafayette, IN, 47907, USA

C.D. Meinhart
Department of Mechanical and Environmental Engineering,
University of California, Santa Barbara, CA, 93106, USA

K. Takehara
Department of Civil Engineering, Kinki University,
Higashi-Osaka 577-8502, Japan

The authors would like to thank Mr. Daniel Laser and Prof. Thomas Kenny of the Mechanical Engineering Department of Stanford University for the use of their silicon microchannel system, and ACLARA BioSciences for the use of several acrylic microchannel systems. Shankar Devasenathipathy is supported by an Agilent Technologies PhD fellowship. This research was supported by the Defense Advanced Research Projects Agency under contracts F33615-98-1-2853 and F30602-98-2-0178, and by the National Science Foundation under Grant No. CTS-9874839.

Symbols

NA	numerical aperture of objective lens
n	refractive index of immersing medium
ϕ	half-angle of the collection cone
λ	wavelength
M	magnification of objective lens
d_s	diameter of point spread function
d_p	particle diameter
d_e	image diameter of particle
δz	depth of field of objective
δz_m	measurement depth
Δt	time spacing between laser pulses
δt	exposure time
μ	dynamic viscosity of fluid
κ	Boltzmann constant
T	temperature
D	diffusion coefficient
u, v, w	x-, y-, z-components of time-averaged velocity
Δx, Δy, Δz	displacements along x-, y-, and z-dimensions
σ_x, σ_y	root-mean-square diffusion distances in the x- and y-dimensions
ε_x, ε_y	relative error caused by Brownian motion in the x- and y-dimensions
p	probability density function
x_0, y_0	location of center of particle image
σ	standard deviation (representative radius) of particle image
r	cross-correlation coefficient
c_t	correlation coefficient threshold

1 Introduction

The advent of micro-electromechanical systems (MEMS) technology has made possible the fabrication of complex fluid flow systems with characteristic dimensions in the range of 1–1000 μm. Microscale flow system technology (microfluidics) is being applied to the development of systems that perform chemical analyses on microchips, low volume flow rate drug dispension devices, fluidic logic systems, and inkjet printer devices (Gravesen et al. 1993;

Brody and Yager 1996). A review of high-resolution flow visualization and quantification techniques (Meinhart et al. 1999a) suggests that micro-PIV provides a practical method of obtaining micron-resolution velocity measurements in microfabricated channels. Micro-PIV combines epifluorescent microscopy and specialized image interrogation algorithms to provide a robust method for measuring velocity fields in microfluidic systems. With or without particle-tracking velocimetry (PTV), micro-PIV provides a diagnostic tool to probe velocity fields in microfluidic systems with high spatial resolutions. Santiago et al. (1998) demonstrated the first application of micro-PIV with fluorescent seed particles by measuring the velocity field around a 30-μm obstacle within a simple glass Hele–Shaw cell. Meinhart et al. (1999b) presented PIV measurements of a pressure-driven flow field in a high-aspect-ratio rectangular cross-section (30 μm×300 μm) glass microcapillary. Ovryn (2000) presented a model for predicting the three-dimensional forward scatter from nonfluorescent particles as applied to PIV. Forward scatter measurements in microfluidic devices are difficult to realize in microchannels, where optical quality surfaces are restricted to one side of the microfluidic system. For example, channels isotropically etched in glass do not have the optical quality needed for particle-based measurements. An additional advantage of fluorescence imaging is the higher signals obtainable by removing scatter from the walls of the microchannel. Meinhart and Zhang (2000) applied PIV to study the flow field in a commercially available inkjet printhead. Singh et al. (2001) demonstrated that liposomes could be alternatively used as fluorescent markers, in addition to the latex microspheres typically used for PIV measurements. Irisawa et al. (2001) recently reported PIV measurements to study mixing in a T-shaped microchannel. Given this recent surge in PIV measurements in microfluidic devices, accurate validation of the technique is critical. One method of validation is to obtain PIV measurements in a well-characterized geometry while obtaining simultaneous measurements of the mass flow rate and/or pressure drop.

In addition to PIV, the application of PTV to microchannel flows offers several advantages. For example, PTV measurements allow the study of dynamics of Brownian particles in the presence of velocity gradients (Batchelor 1976). A second application of PTV is the measurement of temperature fields through the quantification of the Brownian motion of the particles. For example, Hohreiter et al. (2002) showed the application of PIV to measure temperature fields in microchannels. A third application is in microchannel flows driven by the application of electric fields. In such flows, PTV can be used to quantify particle-to-particle differences in electrophoretic drift mobilities and to quantify channels with varying electroosmotic wall mobility (Devasenathipathy et al. 2002). In the current work, we apply both micro-PIV and PTV to obtain nonintrusive measurements of velocity fields within channels micromachined using standard lithographic mask and etching technologies, and we present detailed comparisons of these measurements to both analytical and numerical predictions of velocity fields. We compare the results obtained using micro-PIV alone versus a combination of micro-PIV and PTV for the flow at a cross-channel intersection. The results presented are also a verification of the applicability of two-component micro-PIV measurements to a weakly three-dimensional flow.

2 Theory

2.1 Particle imaging

The characteristics of the particle imaging system largely determine the achievable resolution in a micro-PIV system. Two parameters that characterize the microscope-based imaging system are the total magnification and the numerical aperture of the objective lens. For a 60×magnification objective lens with a numerical aperture of 1.4, following the arguments of Santiago et al. (1998), the image diameter d_e for 500-nm diameter spherical particles is 42 μm. The image diameter projected back into the flow field (using ideal ray optics) is 700 nm. The projected image function limits the achievable resolution of the interrogation system. The accuracy associated with a measurement of a displacement in the streamwise direction is a strong function of the accuracy associated with determining the location of the center of each of the particle images. By resolving the particle image over an area in the detector that is 3 to 4 pixels across, the uncertainty associated with determining the center of the cross-correlation peak is approximately one-tenth of the particle-image diameter (Prasad et al. 1992). In the current work, this translates to an uncertainty of 70 nm in the object plane. Improvements on PIV correlation signal-to-noise ratio (and subsequently spatial resolution) can be obtained for time-averaged or phase-averaged velocity data by averaging a series of correlation functions prior to locating the signal peak in the correlation domain (Meinhart et al. 2000a). This method allows one to obtain reliable measurements, even when only two to three particles are sampled in an interrogation spot at any one time.

2.2 Particle size and dynamics

Particle size is an important consideration in any particle-tracking method. Particles should be small compared to the dimensions of the microfluidic channels and should be much smaller in size than the distance over which significant spatial velocity gradients are to be measured. To meet the first criterion, we use particles less than 1% of the hydraulic diameter of the microchannel. Another important consideration is the optical signal produced by the particles. The particles should be large enough to be visible above background noise without producing unnecessarily large images. Large particle images limit the spatial resolution of the velocity measurements.

Inertial particle effects (Goldstein 1996) are typically not important in microscale liquid flow applications. In the current work, our 500-nm diameter polystyrene spheres provide a particle response time of 10^{-8} s.

Santiago et al. (1998) presented a brief one-dimensional analysis of the effects of Brownian motion on velocity measurement uncertainty. Brownian motion is

the random thermal motion of a particle suspended in a fluid (Probstein 1994). The motion results from collisions between fluid molecules and suspended microparticles. The velocity spectrum of a particle from Brownian motion consists of frequencies too high to be resolved fully and is commonly modeled as Gaussian white noise (Van Kampen 1997). A quantity more readily characterized is the particle's average displacement after many velocity fluctuations. For time intervals Δt that are much larger than the particle inertial response time, the dynamics of Brownian displacement are independent of inertial parameters such as particle and fluid density. Furthermore, the mean square distance of diffusion is proportional to $D\Delta t$, where D, the Stokes–Einstein diffusion coefficient of the particle (Einstein 1905) is given by $\kappa T/(3\pi\mu d_p)$.

The random displacements can be described by the following three-dimensional (Gaussian) probability density function

$$p(x,y,z) = \frac{\exp[-(x^2+y^2+z^2)/4D\Delta t]}{(2\pi)^{3/2}(2D\Delta t)^{3/2}}, \tag{1}$$

and the displacements in the x-, y-, and z-directions are statistically independent random variables.

In the micro-PIV technique presented here, particle displacements are determined by tracking of particle images on a two-dimensional image plane. Therefore, the probability density function of the imaged particle displacements with respect to the background flow can be described by an integration of Eq. (1) along the optical axis z

$$p(x,y) = \int_{-\infty}^{\infty} p(x,y,z)\mathrm{d}z = \frac{\exp[-(x^2+y^2)/4D\Delta t]}{4\pi D\Delta t}, \tag{2}$$

where the coordinates x, y, and z are taken to be displacements with respect to the local fluid flow, and the local fluid flow is assumed constant throughout the region over which the Brownian particle diffuses (i.e., the particle is assumed to sample a region of low velocity gradient). The coordinates x and y are defined to be on the image plane, and any image aberration is ignored here. In practice, Eq. (2) is an approximation to the imaged particle displacement distribution since particles may leave the measurement volume during the interval Δt. Therefore, the two-point probability density function described by Eq. (2) can be interpreted as being valid for cases where $\Delta z = w\Delta t < \delta z_m$, where w is the z-component of velocity.

Brownian displacements cause particle trajectories to fluctuate about the pathlines of the flow field. Assuming the flow field is steady over the time of measurement and the local velocity gradient is small, the imaged Brownian particle motion can be considered a fluctuation about a flow streamline that passes through the initial particle location. The x and y displacements of an ideal non-Brownian particle following the streamline over a time Δt are given by $u\Delta t$ and $v\Delta t$, respectively, where u and v are the x- and y-components of the time-averaged local velocity. The relative error incurred by imaging Brownian displacements in a two-dimensional measurement of the x- and y-components of particle velocity is given as

$$\varepsilon_x = \frac{\sigma_x}{\Delta x} = \frac{1}{u}\sqrt{\frac{2D}{\Delta t}}, \tag{3a}$$

$$\varepsilon_y = \frac{\sigma_y}{\Delta y} = \frac{1}{v}\sqrt{\frac{2D}{\Delta t}}. \tag{3b}$$

This Brownian error establishes a lower limit on the desired measurement time interval since, for shorter times, the measurements are dominated by uncorrelated Brownian motion. For situations where the quantities described by Eq. (3a) are significant, the particle velocity can be thought of as an arithmetic sum of the fluid velocity and the fluctuating Brownian component. These quantities (ratios of the root-mean-square fluctuation to average displacement over time Δt) describe the relative magnitudes of the Brownian motion and will be referred to here as Brownian intensities. The errors estimated by Eq. (3b) show that the relative Brownian intensity error decreases as the time of measurement increases. Larger time intervals produce flow displacements proportional to Δt, while the root mean square of the Brownian particle displacements grow as $\Delta t^{1/2}$. In practice, Brownian motion is an important consideration when tracing 50 to 500 nm particles in flow field experiments with flow velocities of less than about 1 mm/s. For a velocity on the order of 0.5 mm/s and a 500-nm seed particle, the lower limit for the time spacing is approximately 100 μs for a 20% error due to Brownian motion. This error can be reduced both by averaging over several particles in a single interrogation spot and by ensemble averaging over several realizations. The diffusive uncertainty decreases as $1/\sqrt{N}$, where N is the total number of particles in the average (Bendat and Piersol 1986). A discussion on the role of Brownian motion in micro-PIV measurements may also be found in Olsen and Adrian (2000a).

In addition to the Brownian intensity error associated with particle displacement measurements, the Brownian motion incurred during the exposure time δt may also be important in determining the particle location. For example, a 50-nm particle in water at room temperature will have a root-mean-square displacement of 300 nm if imaged with a 10 ms image integration time. For this particle image, the Brownian displacements projected into the image plane during the time of exposure are on the order of the image size (given the best available far-field visual optics with a numerical aperture of 1.4). This random displacement during image exposure can increase the uncertainty associated with estimating the particle location. For low velocity gradients, the centroid of this particle image trace is an estimate of the average location of the particle during the exposure. This particle location uncertainty is typically negligible for exposure times where the typical Brownian displacement in the image plane is small compared to the particle image diameter or the value of the diffusion time $d_e^2/(4DM^2)$ is much greater than the exposure time. In our set up, $d_e^2/(4DM^2)$ is 300 ms and our exposure time is 10 ns.

2.3
Particle tracking algorithms

Cross-correlation PIV is discussed in detail by Raffel et al. (1998). A PIV bibliography by Adrian (1996) lists over 1,200 references describing PIV methods. More recently, interest has been focused on the application of PIV to fluid flow in microfluidic devices. The Reynolds numbers for these flows are typically low, and the flows are usually steady or periodic. Though the fluid flow is itself laminar, the Brownian motion from the diffusion of the submicron seed particles contributes to the measured velocity field. Since Brownian motion at any measurable time scale is uncorrelated, we can, for steady flow fields, time average the velocity field or time average the two-dimensional cross-correlations during interrogation. In the case of quasi-steady flow fields that vary slowly over a given time, the time average must be performed over a period much smaller than the time scale of the flow. Time averaging is generally not appropriate in rapidly varying, unsteady (aperiodic) velocity fields. In such flow fields, one can take advantage of the fact that the Brownian displacements of different particles in the flow field are uncorrelated in space (which is true for realistic particle densities of less than 1% by volume). As such, spatial averaging of measured flow velocities can be used to reduce uncorrelated Brownian noise. Spatial averaging can be accomplished by convolving the velocity field with a Gaussian kernel, which reduces the spatial resolution of the velocity measurements but preserves the measurement's temporal resolution. The spatial and temporal resolutions of particle tracking systems are therefore strongly coupled so that, given a series of images, spatial resolution can be sacrificed for temporal resolution and vice versa.

For the experiments reported in this work, we applied a two-frame digital cross-correlation PIV interrogation code designed to analyze low Reynolds number flows. The PIV algorithm employs time or phase averaging of particle image data correlation functions to increase the signal to noise of the measurement (and subsequently spatial resolution). The code implements an adaptive central difference scheme that is second order accurate in time (Wereley and Meinhart 2001). A typical method for increasing the resolution of PIV measurements is super-resolution PIV (Keane et al. 1995). In this technique, correlation/PIV analyses are first used to determine the average velocity of groups of particles within interrogation regions. This spatially averaged information is then used by a PTV algorithm to determine the displacement of individual seed particles. Several approaches have been adopted to track individual particles in flow fields with high seeding density (Guezennec et al. 1994; Stitou and Reithmuller 2001; Cowen et al. 2001; Ohmi and Li 2000). The super-resolution PIV algorithm presented in our paper is based on Kalman filtering for prediction of the particle trajectory and χ^2 testing for validation of particle identification (Takehara et al. 2000). An estimate of the velocity field is obtained from PIV, and individual particle images are identified and located by a particle mask correlation method. The velocity of each particle is then interpolated, and this velocity is used as a predictor for the particle information in the next image by Kalman filtering. An iterative procedure is implemented until the number of particle pairs matched is maximized.

2.4
Measurement depth for micro-PIV and PTV

In micro-PIV, the measurement domain is defined by the relatively small depth-of-field of a high numerical aperture lens. Meinhart et al. (2000b) and Olsen and Adrian (2000b) present estimations of the effective measurement volume depth δz_m applicable to micro-PIV. For the data presented here, we apply the estimate of δz_m given by the model of Meinhart et al. (2000b), which takes into account the effects of diffraction, geometrical optics, and the size of the particle to the correlation functions used in micro-PIV to calculate velocity. δz_m is 2.2 μm for a 60× magnification oil-immersion objective with a 500-nm diameter particle. Because the correlation function scales as the square of the intensity, particles beyond this distance from the focal plane have a negligible effect on the velocity measurements in micro-PIV (Olsen and Adrian 2000b).

Next, we estimate the measurement depth for the PTV measurements. An important consideration for the application of PTV analysis is the identification of particles from images. Since volume illumination is typically used to image microchannels, depth-resolved PTV measurements are achieved by extracting in-focus particle images. In our work, we accomplish this using a particle mask convolution analysis (Takehara and Etoh 1999). A particle mask approximates an "ideal" particle image as a two-dimensional Gaussian distribution template with a standard deviation σ. The cross-correlation coefficient between the particle mask centered at (x_0,y_0) and the interrogation region in the particle image plane is normalized to correct for nonuniformities in peak brightness of the particle images, which might result from a nonuniform loading of the fluorescent dye onto the latex particles. The point response function for the lens system is an Airy distribution function in the image plane, which is well approximated as a Gaussian. We define the measurement depth δz_m criterion for particle identification for PTV measurements as $r(x,y;\delta z_m)>c_t$. The correlation array r is binarized to denote particle locations. Regions where $r \leq c_t$ are set equal to zero, while regions above c_t are set equal to unity. The choice of c_t and quantification of δz_m for the current experiments is discussed in Sect. 4.1.

3
Experimental setup

3.1
Imaging/recording setup

A schematic of the experimental setup is shown in Fig. 1a. The imaging system consisted of a epifluorescent inverted microscope (Nikon TE300) with illumination provided by dual Nd:YAG lasers (New Wave, Minilase System). In these experiments 60× water and oil immersion objectives applicable to the flow systems under study were used. A 532-nm laser pulse was transmitted through an optical fiber into a custom-built fluorescence color filter assembly.

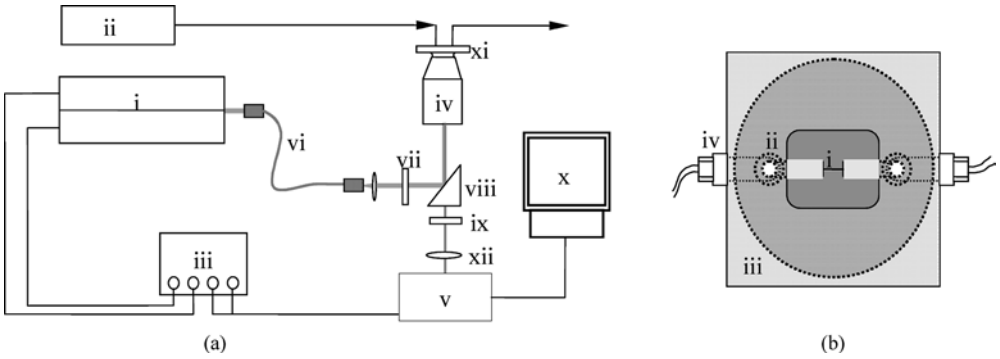

Fig. 1. Experimental setup: **a** Schematic of the PIV setup including dual-head doubled Nd:YAG laser, *i*; syringe pump used to pump liquids, *ii*; timing electronics for control of laser and camera, *iii*; oil immersion objective, *iv*; interline-transfer CCD camera, *v*; liquid-filled optical fiber, *vi*; fluorescence excitation filter, *vii*; dichroic beamsplitter, *viii*; emission color filter, *ix*; computer with frame grabber, *x*; microfluidic test section, *xi*; demagnifying lens (for larger field of view), *xii*. **b** Schematic of the test section showing microchannel etched into a silicon wafer, *i*; fluid reservoir, *ii*; acrylic interconnect fixture, *iii*; compression fittings, *iv*

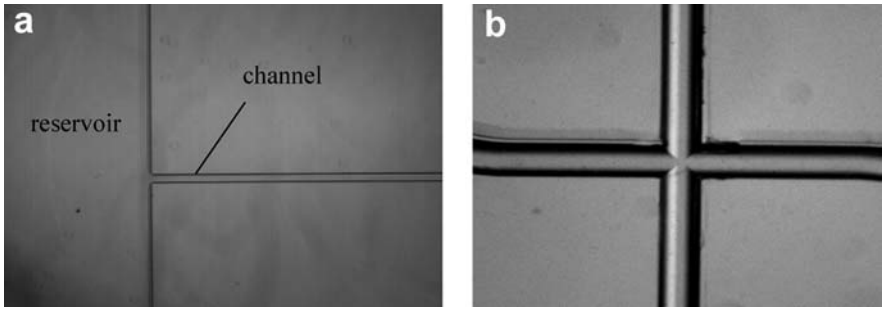

Fig. 2. Images of the two microchannel systems used in the experiments: **a** Straight channel etched in silicon and emptying into a large reservoir (*on left*). **b** Intersection of two channels embossed in an acrylic substrate

The optical fiber (Oriel Instruments) is a single-fiber lightguide with a liquid core and plastic cladding, which illuminates the entire volume of the microchannel test sections. The optical fiber allows easier sharing of the laser source between several experimental rigs and lowers the coherence length of the laser illumination (which helps avoid speckle in particle images). The microscope's color filter assembly consists of a 532-nm clean-up exciter filter, a dichroic beamsplitter with a cut-on wavelength of 545 nm, and a barrier emission filter transmitting wavelengths longer than 555 nm. The 500-nm diameter particles used for the reported experiments have a specific gravity of 1.06 and a diameter distribution with a standard deviation of less than 5% of the mean (Haughland 1996). The particles were supplied by Molecular Probes (Eugene, OR) and are doped with a fluorescent dye that was excited at a peak wavelength of 540 nm and emitted at a 560-nm peak. The images were recorded using a cooled inter-line transfer CCD camera (Princeton Instruments Micromax) with a 1300×1036 pixel array and 12-bit read-out resolution. Prototype microfluidic devices were fabricated in both silicon and acrylic. The description of each setup is provided in the following two sections.

3.2 Silicon channel

A schematic of the silicon channel test section is shown in Fig. 1b. The silicon microchannel system was fabricated from a <100> single-crystal silicon wafer and contains a microchannel 1-cm long by 100-μm wide and 107-μm deep. The microchannel was connected to two reservoirs 5-mm wide and 107-μm deep. The system was fabricated using deep reactive ion etching (Bosch process). A predrilled 500-μm thick Pyrex wafer was anodically bonded to the silicon wafer to seal the microchannel and reservoirs while permitting optical access for flow visualization. The resulting closed microchannel had a hydraulic diameter of 103 μm. The length-to-hydraulic diameter ratio for the silicon channel was 97. An image of the straight channel etched in silicon is shown in Fig. 2a. This flow channel test section was then clamped into an acrylic interconnect fixture fitted with O-rings that permitted interconnection with standard laboratory tubing. A 60× magnification water immersion lens with a numerical aperture of 0.9 and working distance of 2 mm was used for imaging the seeded flow in the silicon channel. Pressure measurements at the inlet to the fixture were made using a pressure transducer (Validyne DP15). The pressure at the exit of the microchannel system was atmospheric. A syringe pump (Harvard Apparatus Ultra-High Pressure PHD 2000) was used to fix the volumetric flow rate through the channel.

3.3 Acrylic channel system

The acrylic channel test structures used here were fabricated by ACLARA BioSciences. These microchannels are embossed on an acrylic substrate and have the D-shaped cross-section typical of an isotropic etch (depth at centerline: 50 μm, top width: 120 μm). A 115-μm thick acrylic sheet thermally laminated to the top of the channels acted as an optical cover-slip and the top wall of the channels. An image of the cross-channel intersection embossed in

acrylic is shown in Fig. 2b. The flow in these microchannels was driven using the hydrostatic pressure head of liquid columns established in reservoirs mounted at the ends of the microchannels. The seeded flow field was imaged with a plan achromat 60× oil immersion objective lens with a maximum numerical aperture of 1.4.

4
Results and discussion

4.1
Calibration experiments for measurement depth

A set of control experiments was performed to estimate the effective measurement depth of the PTV measurements. Particles with diameter 500 nm were placed on a glass slide and imaged with a 60× oil immersion objective lens. Images of immobile fluorescent particles were acquired at various distances from the focal plane. For immobilization, particles are dried onto (adsorbed on) a glass slide. The particle is then immersed in silicone oil to match the index of refraction of the glass slide. In this calibration, particle image intensities are normalized by the maximum intensity value and the representative particle radius for the particle mask σ was chosen to be 2 pixels. Particle images were obtained at six known distances from the focal plane and one at the focal plane. The stage was traversed in increments of 1 μm, and particle images were acquired at these locations. A positive displacement corresponds to a particle that is closer to the objective. Figure 3 shows the cross-correlation coefficient for these seven particle images with our Gaussian mask. The decay of the cross-correlation coefficient is, as expected, not symmetric about the focal plane since particle images are also not symmetric about this plane (Inoue and Spring 1997). Plotted along with the experimental data is a theoretically computed correlation coefficient for the same set of experimental conditions. The theoretical particle image is generated by convolving the three-dimensional diffraction pattern of a point source (Meinhart et al. 2000b) with the geometric image of the particle on the image plane. The correlation coefficient was then computed by convolving this theoretical particle image at different out-of-focus distances with the Gaussian particle mask. Computed values are reported for increments of 0.5 μm. The cross-correlation coefficient threshold can be used as a tuning parameter to choose the effective depth of the measurement volume for the particle identification algorithm. For our study, we chose a correlation coefficient value of 0.7 as the threshold. Applying the threshold criterion described earlier to the experimental data of Fig. 3 results in a measurement depth δz_m of approximately 2 μm.

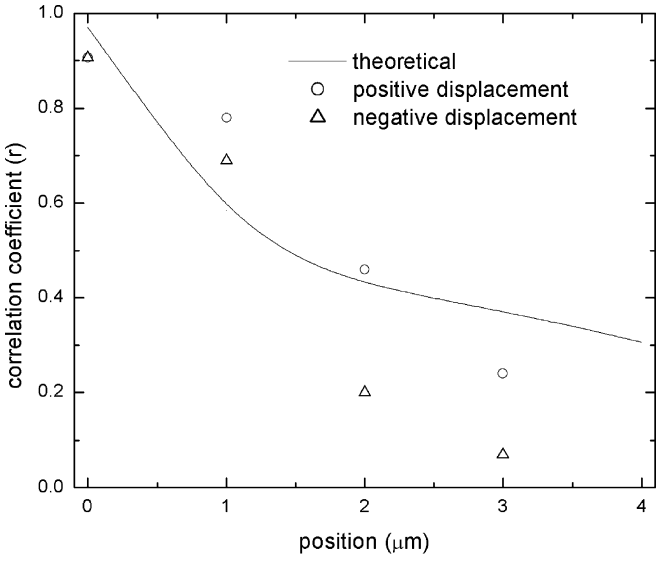

Fig. 3. Calculated and predicted particle image cross-correlation coefficients plotted against the magnitude of the distance from the focal plane of the objective. The *solid line* is a theoretical prediction obtained by convolving the theoretical out-of-focus image with a Gaussian particle mask. The *data points* are obtained by convolving actual particle images obtained at seven distances from the focal plane (spanning from −3 to 3 μm). The theoretical correlation coefficient assumes an ideal, aberration-free lens and is therefore symmetric for positive and negative displacements from the focal plane, while the actual data is asymmetric

4.2
Silicon channel

An initial calibration experiment was conducted to investigate the steadiness of the source pressure and accuracy of the flow rate provided by the syringe pump. In this work, a tube with a hydraulic resistance equivalent to that of the test setup was attached to the outlet of the syringe pump while the pump maintained the flow rate conditions reported above. The fluctuations in the source pressure were found to be ±2% of the mean for a 95% confidence interval. The flow rate of the system was verified by weighing the effluent liquid from this calibration system. Assuming negligible evaporation rates, the syringe pump volume flow rate fluctuations were less than 3% of the desired value.

Figure 4 shows the velocity vector field in the rectangular cross-section silicon microchannel. The flow rate from the syringe pump was maintained at a constant 1.0×10^{-10} m^3/s. PIV measurements were obtained 0.75 cm downstream of the entrance into the channel where the flow is fully developed. The gage pressure at the inlet to the microchannel system was 263 Pa. The measurement volume is located 54 μm from the top wall. The data in this plot were obtained with a time delay of 250 μs between image pairs. The correlation functions of ten image pairs were used. On average, the PIV interrogation regions used here each contained about three particles. The Reynolds number of these flows based on hydraulic diameter and area-averaged velocity is one. The interrogation regions for the measurements shown in Fig. 4 were 128 by 64 pixels in the horizontal and vertical directions, respectively. The velocity measurements show the characteristic, approximately parabolic velocity field for fully developed pressure-driven liquid flow in a rectangular microchannel. The uniformity of vectors along the streamwise direction shows the fully developed flow. Measurements were obtained to within 2 μm of each wall. The solid line is the analytical solution for Newtonian flow in a rectangular channel (White 1991). The analytical

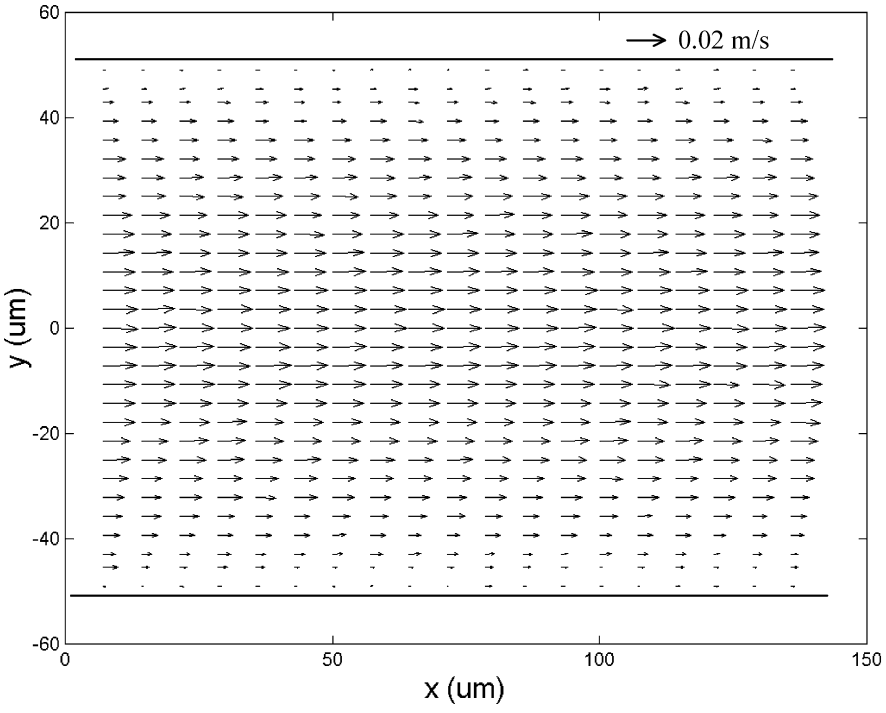

Fig. 4. Velocity field measurement in straight channel section shown in Fig. 2a. The ensemble-averaged velocity-vector field is measured in a rectangular channel (100-μm wide by 107-μm deep, fabricated through deep reactive ion-enhanced etching in silicon). A water immersion lens (M=60; NA=0.9; WD=2 mm) was used to image the seeded flow field. The flow is pressure driven with a syringe pump delivering 10^{-10} m^3/s

solution was determined using the experimentally determined value of the volumetric flow rate provided by the syringe pump. The PIV measurements, averaged over streamlines, are plotted in Fig. 5. The error bars show the standard deviation of the 19-column ensemble over which the averaging was performed. The discrepancy between our PIV measurements and the predicted velocities is less than 3% throughout the field except for the measurements closest to the wall. For the two data points closest to the walls of the channel, the measurements were 6% higher than the predicted velocities. The over-prediction of velocity for distances within one interrogation window of the wall is probably due to near-wall measurement effects. Techniques to improve PIV measurements in regions very close to interfaces are discussed by Tsuei and Savas (2000).

For completeness, we also compared the measurements to velocities predicted using the measured (inlet-to-outlet) pressure drop along the silicon channel. In this case, velocities predicted using the pressure measurements were within 5% of the velocities determined from the flow rate established by the syringe pump. This difference in the predicted velocities may be due, in part, to "second-order effects" such as pressure losses associated with the entrance regions and the fittings for the channel system, which are difficult to measure. For example, an additional 3-Pa pressure drop caused by end effects of the straight channel can be estimated using the correlation suggested by Weissberg (1962). Another limitation on using pressure measurements is the accuracy of our pressure transducer (reported as ±0.25% of the full-scale range by the manufacturer), which is ±2.2 Pa uncertainty for our experiment. For the detailed comparisons shown in Fig. 5, we chose flow rate as our bulk parameter of interest to avoid assumptions regarding these second-order effects.

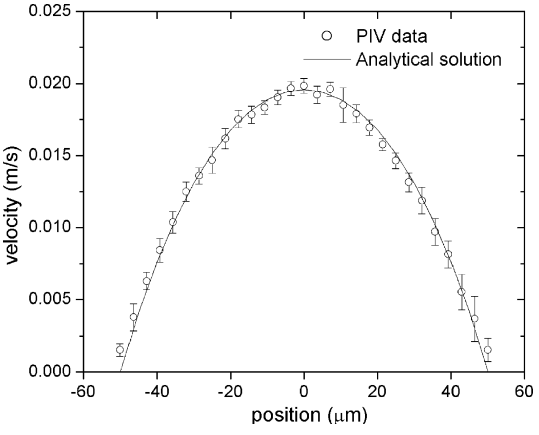

Fig. 5. Comparison between experimental data and analytical solution for flow in a straight channel with rectangular cross section. The data has been averaged along the streamlines. The *error bars* show the standard deviation of the 19-column ensemble over which the averaging was performed. The *solid line* is the analytical solution for Newtonian flow through a rectangular channel

4.3
Acrylic channel system

For the experiments in the acrylic channel, the focal plane was 10 μm from the surface of the channel nearest to the objective (the bottom wall). Figure 6a shows the interrogation location for the acrylic cross-channel system along with the defined coordinate axes. Figure 7a shows the ensemble-averaged velocity-vector field obtained in the region of the intersection of two channels of the acrylic substrate system. The pressure difference between the inlet and outlet of the channel system was 235 Pa. Assuming the pressure losses associated with fully developed flow were

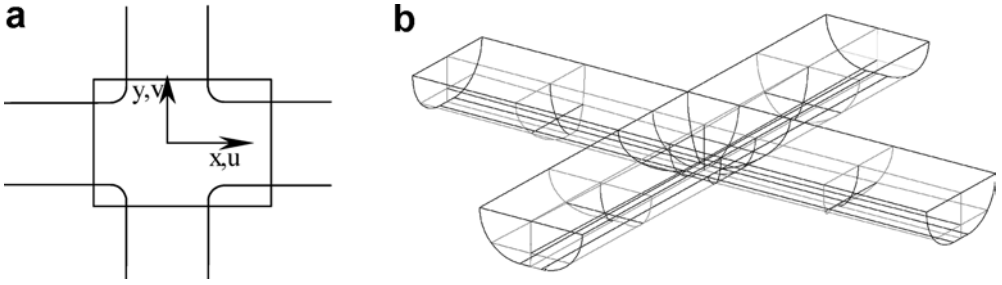

Fig. 6. Intersection region of the cross-channel system: **a** Schematic of intersection showing the imaging plane field of view for the current experiments. **b** Geometry of the numerical model of the microchannel system embossed in acrylic substrate. The channel top width is 120μm with a 50-μm depth at the centerline

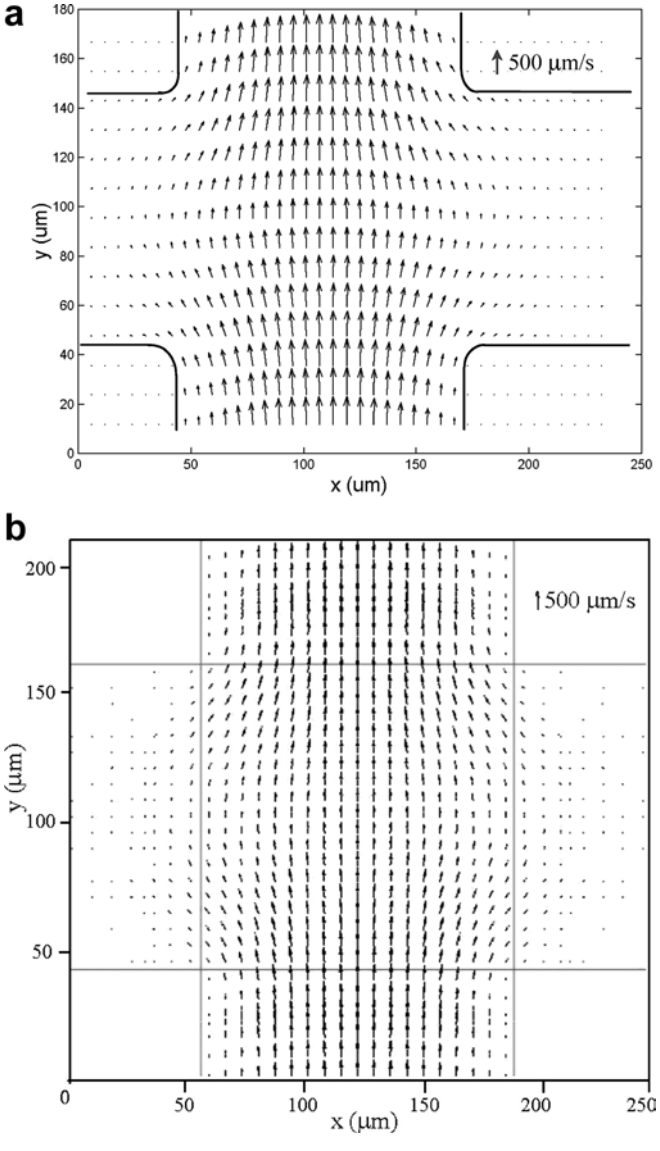

Fig. 7. Velocity field at the intersection of a cross-channel system, the schematic of the measurement location is shown in Fig. 6a. **a** Ensemble-averaged velocity vector field for pressure-driven flow at the intersection of two cross-channels. **b** Velocity vector field from a numerical simulation at the same plane where the measurements were conducted. The geometry utilized in the numerical scheme is shown in Fig. 6b. Numerical simulations for pressure-driven flow for this geometry were performed with ACE+ software

much larger than secondary losses in the system (e.g., development regions and the intersection), the pressure gradient in the straight portions of the channel was 4.0 Pa/mm. The pressure-driven flow is directed from the bottom of the figure to the top, and the maximum velocity is 660 μm/s. The ends of the horizontal channels of the system (1.4 cm from the intersection) were sealed to prevent net flow from the intersection to the side channels. Because the microchannel cross-sections have the D-shape characteristic of isotropic etching, the velocity field in the region of the intersection of these channels is three-dimensional. However, the out-of-plane velocities in the measurement volume are small enough such that the $\delta z_m > \Delta z$ condition described earlier is met. In the current experiments, the maximum out-of-plane displacement of our weakly three-dimensional flows is Δz=0.5 μm and is less than the measurement depth for both the PIV and PTV analyses. The measured velocities are the in-plane components of the weakly three-dimensional velocity field within the measurement volume, as projected onto the plane of the CCD array. The interrogation regions in this case were 128 by 64 pixels in the vertical and horizontal directions, respectively (equivalent to a 23.8 μm by 11.9 μm distance when projected onto the object plane). The time spacing between each pair of images for the cross-channel experiments was 20 ms. The correlation functions of ten image pairs were averaged to obtain this steady flow measurement. The velocity field measurements show the top-down symmetry expected in low Reynolds number flow. The velocity measurements extend to within 5 μm of the wall. We found it difficult to obtain reliable measurements closer to the wall because of the image noise associated with particle light scatter at the wall surface. The sidewalls of the acrylic channels are inclined with respect to the measurement plane (unlike the deep reactive ion-etched silicon microchannels described earlier). The velocities of the bottom-most velocity profile of measurement volume very nearly match the fully developed flow profile. A secondary flow induced in the side channels by the vertical liquid stream decays off to negligible values within 120 μm from the center of the intersection. Figure 7b shows the flow field from simulation results obtained using CFD-ACE+ (CFD Research, Huntsville, AL) code. The model geometry for the numerical predictions, shown in Fig. 6b, replicates the intersection region of the D-shaped cross-section of the channels. The microchannel geometry was verified using measured profiles from a surface profilometer (Tencor AlphaStep). The flow at the intersection was solved numerically with the inlet and the outlet maintained at fixed pressures and zero net flow from the side channels. In Fig. 7b, the theoretical prediction was fit to the experimental values by varying the pressure gradient in the

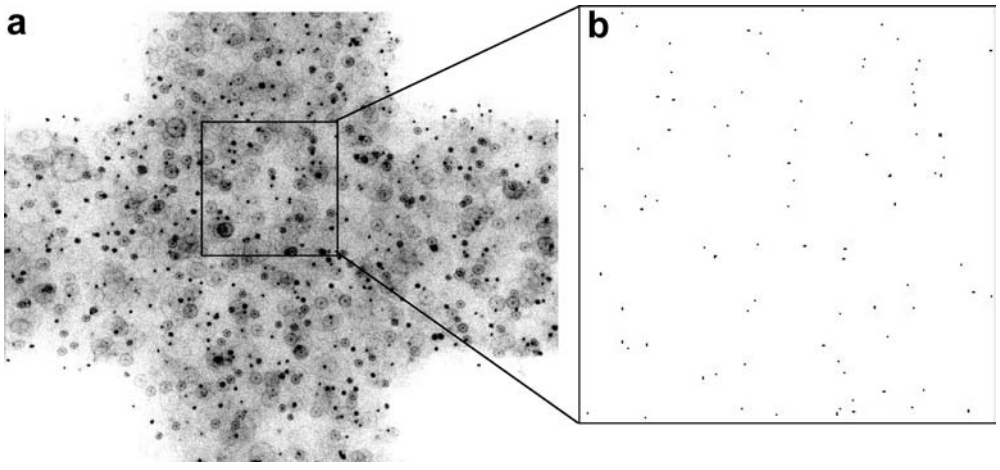

Fig. 8. a Representative raw image (negative, with white corresponding to a minimum intensity value) of the seeded flow field. **b** Binarization of a subregion (again, a negative) using a threshold based on the convolution of the image with the ideal Gaussian particle shape

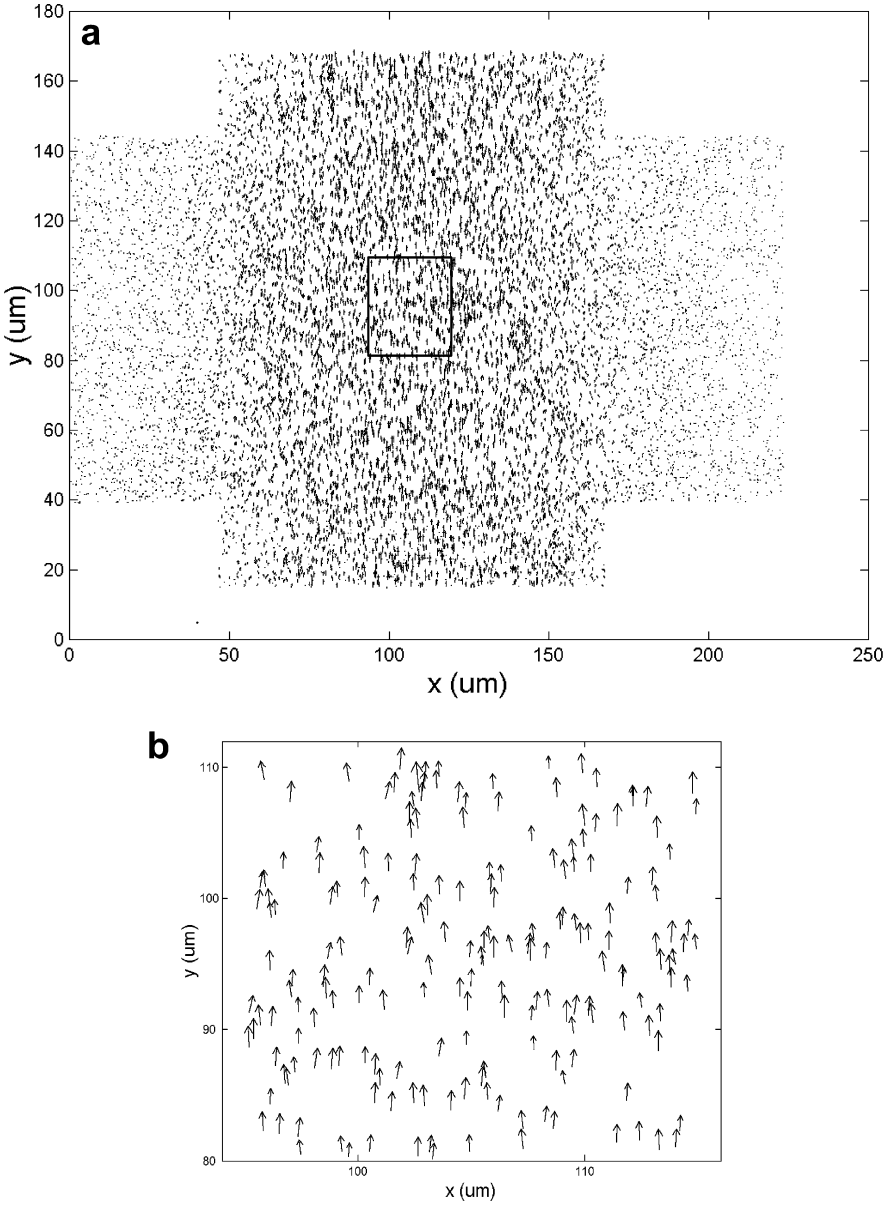

Fig. 9. a Velocity field obtained by applying a combined PIV and PTV analysis to the same images used in the PIV measurements shown in Fig. 7. **b** Velocity vectors in an exploded view of *subregion* shown in Fig. 9a

straight portion of the channel with fully developed flow at the inlet. This best-fit pressure-gradient parameter was 3.8 Pa/mm. This is in good agreement with the approximate pressure gradient measurement of 4.0 Pa/mm described above. The 4.0 Pa/mm estimate was obtained from the pressure difference value, the length of the channel,

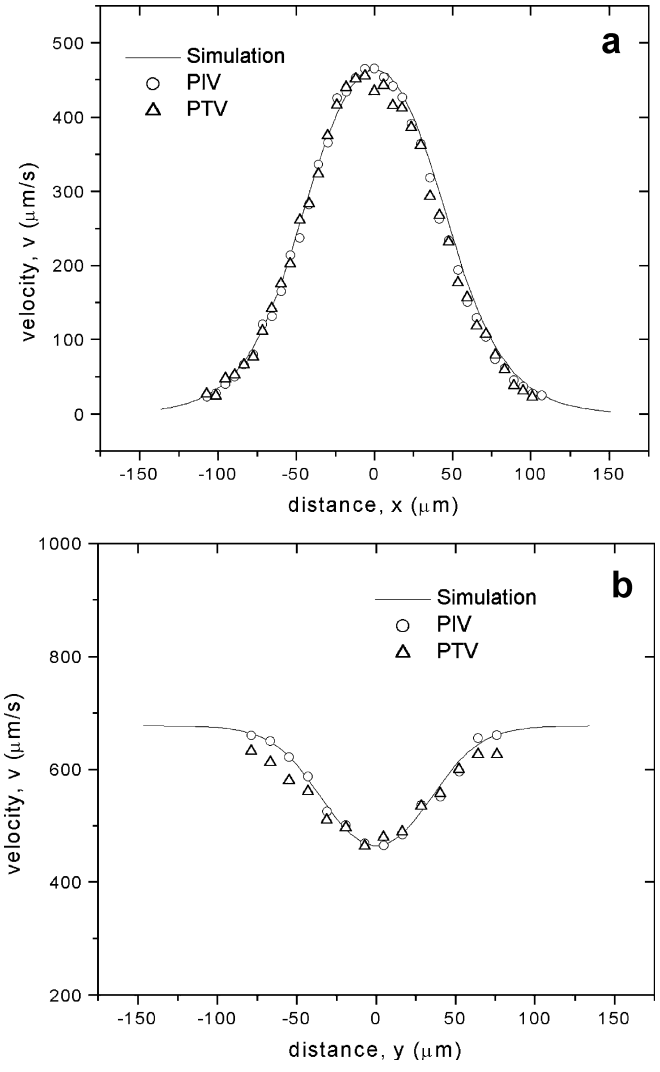

Fig. 10. Comparison of experimental data with numerical predictions for flow at the intersection: **a** Streamwise velocity v against transverse distance x. **b** Streamwise velocity v against streamwise distance y

and the assumption that the secondary pressure losses are much smaller than the fully developed flow losses. The L/D ratio of the straight portions of the channel is 890, and the straight, fully-developed portions of the channel account for approximately 95% of the total flow length.

Figure 8 shows two steps of the particle identification process for a particle field image obtained during flow conditions. A particle mask is convolved with the interrogation area from the flow field (Fig. 8a) and thresholded with the cross-correlation coefficient at 0.7 to yield the binarized image shown in Fig. 8b. The laser pulse energy was chosen such that the particle images were not saturated at any time, since the correlation mask method used here rejects particle images if the particle image intensities saturate the CCD.

Figure 9 shows the result for the data images described above using the combined PIV/PTV analysis. In PIV the quantitative estimation of validity (not the accuracy) of a velocity vector is obtained from the signal-to-noise ratio in the correlation domain. This validation criterion does not apply to the PTV. Neighboring vectors may be used to validate individual particle displacements, but this is under the risk of spatially filtering the velocity field, as pointed out by Stitou and Riethmuller (2001). We apply the χ^2 image tracking validation described by Takehara et al. (2000). As shown in the figure, the velocity field obtained with the PIV/PTV analysis is unstructured, given the random position of validated particle displacements inside the flow field. The main advantage with this combined PIV-PTV analysis is the higher sampling density achieved. The number of vectors obtained by PIV cross-correlation analysis is 480 in the test section, while the number of vectors identified by the super-resolution–Kalman filtering–χ^2 method is 5200, a tenfold increase. Note that the vectors from the PTV analysis are individual particle displacements, randomly positioned in the flow field, and include the Brownian motion component. We can estimate the spatial resolution of the PTV measurements in this system by considering the number density of measurements and the length of particle displacements. For example, along the flow direction, the spatial resolution may be described by the local particle displacement. For the measurements shown in Fig. 9, particle displacements range from negligible values in the side-channels to 10 μm at the centerline. The resolution in the direction transverse to streamlines can be estimated by the mean spacing between valid velocity measurements in that direction. The number density of particle displacements in the test section is 20/100 μm^2 (for the combined data of all ten image pairs) so that we can expect a mean vector spacing on the order of 2 μm. Given enough randomly positioned ensemble-averaged velocity measurements, a lower limit on the spatial resolution achievable with PTV is dictated by the size of the seed particles. For the current work, this limit is approximately 500 nm.

Figure 10 shows the comparison of the experimental data (both PIV and PTV) at the intersection of the acrylic microchannel system with results from a simulation of the velocity field. The randomly located PTV data was interpolated onto the same grid points as the PIV data with a Gaussian convolution scheme that allows the redistribution of the unstructured PTV data onto a regular grid structure (Keane et al. 1995).

The measurements shown in Figs. 5 and 10 compare very well with the predicted velocity distributions. This agreement shows that a volume illumination may be used in conjunction with the depth of field of the objective lens to resolve two-dimensional velocity measurements in at least weakly three-dimensional velocity fields using micro-PIV. The agreement of both the straight channel and the intersection flow measurements with theory support the expected result that the liquid microflow at these scales is well described by macroscale flow theory (Sharp et al. 2001).

5 Conclusions

PIV and PTV were applied to measurements of velocity fields in microfabricated fluidic channels with characteristic dimensions of 20–150 μm. The technique uses epi-fluorescent microscopy and a CCD camera to image 500-nm diameter fluorescently tagged polystyrene particles. An analysis for estimating the error incurred because of

Brownian motion in two-component velocity measurements in three-dimensional flows was presented. The particle tracking system was used to provide velocity measurements in pressure-driven flow fields in channels fabricated in silicon and acrylic. These microchannel systems have hydraulic diameters of 103 μm and 66 μm, respectively. Measured flow velocity fields compare very well with theoretical calculations of the viscous flow in these microchannels. Quantitative measurements of velocities in both one-dimensional and three-dimensional flow fields were presented and compared with analytical and numerical predictions. The agreement between the absolute velocity measurement values and the values predicted using bulk flow properties and theory support the view that liquid flow in microchannels of order 50-μm geometry are well approximated by macroscale (continuum) flow theory for the channel substrates investigated here. Results from a combined PIV–PTV analysis were presented for the flow at the cross-channel intersection for this microfluidic geometry. An enhanced spatial resolution is obtained by tracking individual particles in the images with PTV/PIV providing over ten times more velocity measurements per unit area than PIV alone.

References

Adrian RJ (1996) Bibliography of particle image velocimetry using imaging methods: 1917–1995. TAM Report 817, UILU-ENG-96-6004, University of Illinois at Urbana-Champaign, Urbana

Batchelor GK (1976) Brownian diffusion of particles with hydrodynamic interaction. J Fluid Mech 74:1–29

Bendat JS, Piersol JG (1986) Random data: analysis and measurement procedures. Wiley, New York

Brody JP, Yager P (1996) Biotechnology at low Reynolds numbers. Biophys J 71:3430–3441

Cowen EA, Chang KA, Liao Q (2001) A single-camera coupled PTV–LIF technique. Exp Fluids 31:63–73

Devasenathipathy S, Santiago JG, Takehara K (2002) Particle tracking techniques for electrokinetic microchannel flows. Anal Chem 74:3704–3713

Einstein A (1905) On the movement of small particles suspended in a stationary liquid demanded by the molecular–kinetic theory of heat. In: Theory of Brownian movement. Dover, New York, pp 1–18

Goldstein RJ (ed) (1996) Fluid mechanics measurements. Taylor and Francis, Washington

Gravesen P, Branebjerg J, Jensen OS (1993) Microfluidics—a review. J Micromech Microeng 3:168–182

Guezennec YG, Brodkey RS, Trigui N, Kent JC (1994) Algorithms for fully automated 3-dimensional particle tracking velocimetry. Exp Fluids 17:209–219

Haughland RP (1996) Handbook of fluorescent probes and research chemicals. Molecular Probes, Eugene, OR

Hohreiter V, Wereley ST, Olsen MG, Chung JN (2002) Cross-correlation analysis for temperature measurement. Meas Sci Technol 13:1072–1078

Inoue S, Spring KR (1997) Video microscopy: the fundamentals. Plenum, New York

Irisawa G, Ishizuka M, Sato Y, Hishida K, Maeda M (2001) Visualization of convective mixing in microchannel by fluorescence imaging. In: Proc 4th International Symposium on Particle Image Velocimetry, Gottingen, Germany, 17–19 September 2001

Keane RD, Adrian RJ, Zhang Y (1995) Super-resolution particle imaging velocimetry. Meas Sci Technol 6:754–768

Meinhart CD, Wereley ST, Santiago JG (1999a) Micron-resolution velocimetry techniques. In: Adrian RJ et al (eds) Developments in laser techniques and applications to fluid mechanics. Springer, Berlin Heidelberg New York

Meinhart CD, Wereley ST, Santiago JG (1999b) PIV measurements of a microchannel flow. Exp Fluids 27:414–419

Meinhart CD, Wereley ST, Santiago JG (2000a) A PIV algorithm for estimating time-averaged velocity fields. J Fluids Eng 122: 285–289

Meinhart CD, Wereley ST, Gray MHB (2000b) Volume illumination for two-dimensional particle image velocimetry. Meas Sci Technol 11:809–814

Meinhart CD, Zhang HS (2000) The flow structure inside a microfabricated inkjet printhead. J Microelectromech Syst 9:67–75

Ohmi K, Li HY (2000) Particle tracking velocimetry with new algorithm. Meas Sci Technol 11:603–616

Olsen MG, Adrian RJ (2000a) Brownian motion and correlation in particle image velocimetry. Opt Laser Technol 32:621–627

Olsen MG, Adrian RJ (2000b) Out-of-focus effects on particle image visibility and correlation in microscopic particle image velocimetry. Exp Fluids 29:S166–S174

Ovryn B (2000) Three-dimensional forward scattering particle image velocimetry applied to a microscopic field-of-view. Exp Fluids 29:S175–S184

Prasad AK, Adrian RJ, Landreth CC, Offutt PW (1992) Effect of resolution on the speed and accuracy of particle image velocimetry interrogation. Exp Fluids 13:105–116

Probstein RF (1994) Physicochemical hydrodynamics: an introduction. Wiley, New York

Raffel M, Willert CE, Kompenhans J (1998) Particle image velocimetry: a practical guide. Springer, Berlin Heidelberg New York

Santiago JG, Wereley ST, Meinhart CD, Beebe DJ, Adrian RJ (1998) Particle image velocimetry system for microfluidics. Exp Fluids 25:316–319

Sharp KV, Adrian RJ, Santiago JG, Molho JI (2001) Liquid flows in microchannels. In: Gad-el-Hak M (ed) The MEMS handbook. CRC, Boca Raton

Singh AK, Cummings EB, Throckmorton DJ (2001) Fluorescent liposome flow markers for microscale particle image velocimetry. Anal Chem 73:1057–1061

Stitou A, Riethmuller ML (2001) Extension of PIV to super resolution using PTV. Meas Sci Technol 12:1398–1403

Takehara K, Etoh T (1999) A study on particle identification in PTV—particle mask correlation method. J Visualiz 1:313–323

Takehara K, Adrian RJ, Etoh GT, Christensen KT (2000) A Kalman tracker for super-resolution PIV. Exp Fluids 29:S34–S41

Tsuei L, Savas O (2000) Treatment of interfaces in particle image velocimetry. Exp Fluids 29:203–214

Van Kampen NG (1997) Stochastic processes in physics and chemistry. North-Holland, Amsterdam

Weissberg HL (1962) End correction for slow viscous flow through long tubes. Phys Fluids 5:1033–1036

Wereley ST, Meinhart CD (2001) Second-order accurate particle image velocimetry. Exp Fluids 31:258–68

White FM (1991) Viscous fluid flow. McGraw-Hill, New York